

NUMERICAL SIMULATION OF STAR FORMATION BY THE BOW SHOCK OF THE CENTAURUS A JET

CARL L. GARDNER¹, JEREMIAH R. JONES¹, EVAN SCANNAPIECO², AND ROGIER A. WINDHORST²

¹School of Mathematical & Statistical Sciences, Arizona State University, Tempe AZ 85287, carl.gardner@asu.edu, jrjones8@asu.edu

²School of Earth & Space Exploration, Arizona State University, Tempe AZ 85287, evan.scannapieco@asu.edu, rogier.windhorst@asu.edu

ABSTRACT

Recent *Hubble Space Telescope* (*HST*) observations of the extragalactic radio source Centaurus A (Cen A) display a young stellar population around the southwest tip of the inner filament 8.5 kpc from the Cen A galactic center, with ages in the range of 1–3 Myr. Crockett et al. (2012) argue that the transverse bow shock of the Cen A jet triggered this star formation as it impacted dense molecular cores of clouds in the filament. To test this hypothesis, we perform three-dimensional numerical simulations of induced star formation by the jet bow shock in the inner filament of Cen A, using a positivity preserving WENO method to solve the equations of gas dynamics with radiative cooling. We find that star clusters form inside a bow-shocked molecular cloud when the maximum initial density of the cloud is ≥ 40 H₂ molecules/cm³. In a typical molecular cloud of mass $10^6 M_{\odot}$ and diameter 200 pc, approximately 20 star clusters of mass $10^4 M_{\odot}$ are formed, matching the *HST* images.

Keywords: galaxies: active — galaxies: jets — galaxies: star formation — methods: numerical

1. INTRODUCTION

The nearest powerful extragalactic radio source is Centaurus A (Cen A), which is emitted by the active galactic nucleus (AGN) of the elliptical galaxy NGC 5128. Unlike most elliptical galaxies, NGC 5128 hosts a prominent dust lane that is thought to have been created by a recent merger with a gas-rich disk galaxy (Israel 1998), which also provided the fuel for the AGN outburst. At a distance of 3.7 Mpc from the Earth, Cen A provides a unique opportunity to study the evolution of AGN driven radio jets.

Centaurus A is at the center of a relatively low mass $\approx 2 \times 10^{12} M_{\odot}$ galaxy subgroup (Karachentsev et al. 2002), one of two subgroups within the Cen A/M83 galaxy group. The subgroup spans a region ≈ 400 kpc in radius around NGC 5128, which at this close distance covers many degrees in the southern sky. Cen A is similarly impressive at radio wavelengths, showing multiple synchrotron emitting lobes, ranging in scale from a pair of inner lobes at a distance of 5 kpc from the AGN, to a single Northern Middle Lobe at a distance of 25–30 kpc, and to a pair of outer lobes at a distance of 100 kpc from the nucleus (Morganti et al. 1999, Saxton et al. 2001, Feain et al. 2009). Furthermore, the bent morphologies of the jets, as well as their association with X-ray emitting knots and regions of bright optical and UV emission, all suggest a complex history of interactions between the jets and the surrounding gaseous environment (Rejkuba et al. 2001, 2002, 2004, Fassett & Graham 2000, Graham & Fassett 2002, Kraft et al. 2009, Gopal-Krishna & Wiita 2010).

Of particular interest is the connection between the radio features and star formation. Such AGN feedback is widely invoked in theoretical models both to explain the overall history of cosmic star formation, as well as to explain the properties of individual AGN host galaxies and their surroundings. On cosmic scales, it is thought that the primary impact of AGN is to decrease star formation by removing gas from galaxies and heating the gas that surrounds them. Such “negative feedback” is required to explain three key cosmological trends: (i) that the overall star formation rate has dropped since $z \approx 2$, 4 Gyr after the Big Bang (Hopkins & Beacom 2006, Karim et al. 2011); (ii) that the rate of star formation peaked first in the most massive galaxies and later in smaller galaxies (e.g., Cowie et al. 1996, Brinchmann & Ellis 2000, Noeske et al. 2007, Cowie & Barger 2008); and (iii) that galaxy clusters that show rapid gas cooling in their centers do not show evidence of strong star formation (e.g., Peterson et al. 2001, Rafferty et al. 2006, Cavagnolo et al. 2009). Negative AGN feedback in the form of radiatively driven winds and radio jets has been shown to address these questions by (i) providing enough energy to remove and heat the gas that would otherwise form stars below $z = 2$ (Granato 2004, Scannapieco & Oh 2004, Croton et al. 2006); (ii) preferentially reducing star

formation first in large galaxies at early times, and then in smaller galaxies at late times (e.g., Scannapieco & Oh 2004, Scannapieco et al. 2005, Hopkins et al. 2006, Somerville et al. 2008, Johansson et al. 2012, Wurster & Thacker 2013, Costa et al. 2014, Richardson et al. 2016); and (iii) providing the energy to reheat the cooling gas in cold-core galaxy clusters (e.g., Dunn & Fabian 2006, McNamara & Nulsen 2007, 2012, Fabian 2012, Gaspari et al. 2012a, 2012b, Li et al. 2015).

In more limited cases, “positive feedback” from active galactic nuclei may induce star formation by creating expanding rings of star formation around the centers of galaxies, triggered by jet bow shocks (see Fragile et al. 2004, Gaibler et al. 2012, Silk 2013, Zinn et al. 2013, Dugan et al. 2014, Gaibler 2014, Wagner et al. 2015, Dugan et al. 2016). At $z = 3.9$, the galaxy 4C 41.17 has been observed to host a powerful radio jet with strong evidence for induced star formation along the radio axis (Dey et al. 1997, Bicknell et al. 2000). At $z = 0.31$, multi-wavelength observations of the radio source PKS2250-41 suggest that the radio jet in this source has triggered recent star formation within a faint companion. In the galaxy cluster Abell 194, which is 78.7 Mpc away from the Earth, the peculiar galaxy “Minkowski’s Object” (Minkowski 1958) is likely to be experiencing a burst of star formation triggered by the radio jet from the nearby active galaxy NGC 541 (van Breugel et al. 1985, Croft et al. 2006).

In the case of Cen A, two optical filaments with recently formed star clusters are observed near the northern radio jet. Recent *Hubble Space Telescope* (*HST*) observations by Crockett et al. (2012) of the inner filament of Cen A display a young stellar population around the southwest tip of the filament (reproduced in Figure 1 here), with ages in the range of 1–3 Myr. Crockett et al. (2012) argue that the transverse bow shock of the Cen A jet triggered this star formation as it impacted the dense molecular cores of three clouds in the filament. If this view is correct, then the inner filament of Cen A would provide one of the nearest and best measured examples of the positive feedback of AGN activity on the subsequent formation of stars.

As indicated in Figure 1, the jet-induced star formation in the inner filament occurs at some distance from the visible, radio, and X-ray portions of the northern jet, more or less along the (invisible) extension of the X-ray jet (see Figure 1 in Crockett et al. 2012). Note that this latter figure implies that the physical conditions required in the simulations to trigger star formation still hold this far away from the jet, because the inner filament is near the edge of the radio jet. In other words, the jet bow shock is still expanding laterally beyond the region where the jet is visible in radio and X-ray emission. The AGN jet may also be precessing around the central engine on a timescale of approximately 10^7 years, but the effects of the precession are beyond the scope of the current paper.

Sutherland et al. (1993) suggested that radio jet-induced shocks can produce the observed optical line emission from the inner filament. However, Crockett et al. (2012) maintain that such shocks are produced by the bow shock propagating through the diffuse interstellar medium, rather than by the radio jet directly. As the bow shock collides with molecular clouds precipitating star formation in the dense molecular cores, ablation and heating of the diffuse gas result in the observed optical line and X-ray emission. Wagner et al. (2015) found that star formation occurs in dense clouds with diameters greater than about 25 pc, but that bow shock ablation quenches star formation in smaller clouds.

This investigation focuses on jet-induced localized star formation in Cen A in larger molecular clouds with diameters between 130–325 pc, far away (8.5 kpc) from the AGN. To test the hypothesis, we perform three-dimensional (3D) numerical simulations of induced star formation by the jet bow shock in the inner filament of Cen A, using a positivity preserving WENO method to solve the equations of gas dynamics with radiative cooling. The number of star clusters formed, as well as their sizes and masses, are in good agreement with the *HST* observations.

The structure of this investigation is as follows. In Section 2, we describe our numerical methods, radiative cooling model, and initial conditions. In Section 3 we present our simulation results, focusing on the jet evolution and induced star formation by the jet bow shock. These results are discussed further in Section 4, and conclusions are given in Section 5.

2. NUMERICAL SIMULATIONS

2.1. Numerical Methods

We applied the WENO (weighted essentially non-oscillatory) method (Shu 1999)—a modern high-order upwind method—to the equations of gas dynamics with atomic and molecular radiative cooling to simulate the AGN jet and its impact with nearby molecular clouds. The equations of gas dynamics with radiative cooling take the form of hyperbolic conservation laws for mass, momentum, and energy:

$$\frac{\partial \rho}{\partial t} + \frac{\partial}{\partial x_i}(\rho u_i) = 0 \quad (1)$$

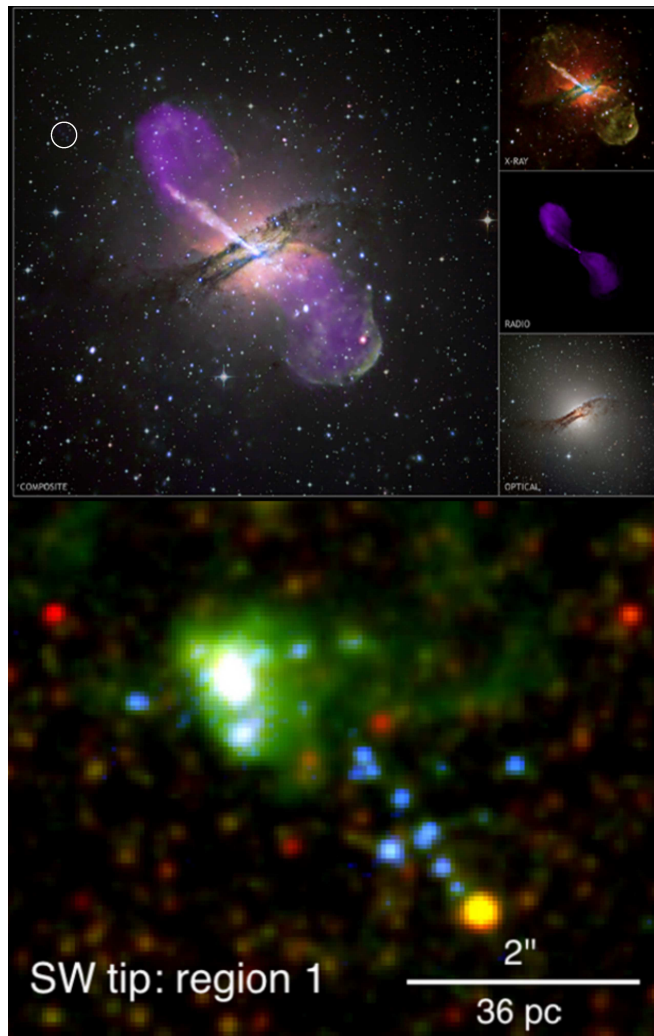


Figure 1. Top panel: Composite of Chandra X-ray image, VLA radio image, and ESO optical image of the Cen A jet and galaxy NGC 5128: X-ray image NASA/CXC/CfA/R. Kraft et al.; radio image NSF/VLA/Univ. Hertfordshire/M. Hardcastle; optical image ESO/WFI/M. Rejkuba et al. A 1 kpc diameter area surrounding cloud A (which is about 200 pc in diameter and contains Region 1) in the inner filament is marked by a white circle. Bottom panel: A zoomed-in *HST* view of Region 1 (Crockett et al. 2012), where numerous young star clusters can be seen as bright blue dots. Region 1 is estimated to contain about $10^5 M_{\odot}$, while the individual clusters are estimated to contain about $10^3 M_{\odot}$ each.

$$\frac{\partial}{\partial t}(\rho u_j) + \frac{\partial}{\partial x_i}(\rho u_i u_j) + \frac{\partial P}{\partial x_j} = 0 \quad (2)$$

$$\frac{\partial E}{\partial t} + \frac{\partial}{\partial x_i} [u_i(E + P)] = -C(n, T), \quad (3)$$

where $\rho = mn$ is the density of the gas, m is the average mass of the gas atoms or molecules, n is the number density, u_i is the velocity, ρu_i is the momentum density, $P = nk_B T$ is the pressure, T is the temperature, and E is the energy density of the gas. Indices i, j equal 1, 2, 3, and repeated indices are summed over. The pressure is related to the other state variables by the equation of state:

$$P = (\gamma - 1) \left(E - \frac{1}{2} \rho u^2 \right), \quad (4)$$

where γ is the polytropic gas constant.

We use a “one fluid” approximation in the simulations, and assume that the gas is predominantly H above 8000 K, with the standard admixture of the other nine most abundant elements He, C, N, O, Ne, Mg, Si, S, and Fe in the interstellar medium; while below 8000 K, we assume the gas is predominantly H_2 , with $n(H)/n(H_2) \approx 0.01$. We make the further approximation that γ is fixed at $\frac{5}{3}$ (the value for a monatomic gas) for simplicity.

Radiative cooling of the gas is incorporated through the right-hand side $-C(n, T)$ of the energy conservation equation (3), where

$$C(n, T) = \begin{cases} n^2 \Lambda(T) & T \geq 8000 \text{ K, for atomic cooling only} \\ nW(n, T) & T < 8000 \text{ K, for H}_2 \text{ cooling only} \end{cases} \quad (5)$$

with the model for $\Lambda(T)$ taken from Figure 8 of Schmutzler & Tscharnuter (1993) for atomic cooling, encompassing the relevant emission lines of the ten most abundant elements in the interstellar medium, as well as relevant continuum processes; and the model for $W(n, T)$ from Figure 4 of Le Bourlot et al. (1999) for H₂ molecular cooling. Both atomic and molecular cooling are actually operative between $8000 \text{ K} \leq T \leq 10,000 \text{ K}$, but atomic cooling is dominant in this range.

We use a positivity preserving (Hu et al. 2013) version of the third-order WENO method (Shu 1999, p. 439) for the simulations (Ha et al. 2005). ENO and WENO schemes are high-order finite difference schemes designed for nonlinear hyperbolic conservation laws with piecewise smooth solutions containing sharp discontinuities like shock waves and contacts. The WENO schemes use a convex combination of all candidate upwind and central stencils, rather than just one as in the original ENO method.

Positivity preserving methods ensure that the gas density and pressure always remain positive (most numerical methods for gas dynamics can produce negative densities and pressures) by limiting the numerical flux. Without the incorporation of the positivity preserving flux limiter, the simulations broke down as soon as the jet bow shock impacted the dense molecular clouds.

Our WENO code is parallelized as a hybrid MPI/OpenMP program, using MPI to distribute the computational grid over multiple compute nodes and localized OpenMP threading to use all cores on a given node.

2.2. Initial Conditions

Parallelized simulations were performed on a $420\Delta x \times 420\Delta y \times 420\Delta z$ grid spanning $6 \times 10^{16} \text{ km} = 1.9 \text{ kpc}$ on a side, where the grid size $\Delta = \Delta x = \Delta y = \Delta z = 4.6 \text{ pc}$. The jet was emitted through a disk-shaped inflow region in the xy plane centered on the z -axis with a diameter of $2 \times 10^{15} \text{ km}$, and propagated along the z -axis with an initial velocity of $4 \times 10^4 \text{ km s}^{-1}$. The simulation parameters at $t = 0$ for the jet, ambient gas, and molecular clouds are given in Table 1. The ambient gas and molecular clouds were initially pressure-matched with the jet.

Table 1. Initial parameters for the jet, ambient gas, and clouds.

Jet	Ambient Gas	Clouds
$n_j = 0.01 \text{ H atoms/cm}^3$	$n_a = [0.02, 0.2] \text{ H atoms/cm}^3$	$n_c = [2, 75] \text{ H}_2 \text{ molecules/cm}^3$
$u_j = 4 \times 10^4 \text{ km s}^{-1}$	$u_a = 0$	$u_c = 0$
$T_j = 10^5 \text{ K}$	$T_a = [5 \times 10^3, 5 \times 10^4] \text{ K}$	$T_c = [7, 250] \text{ K}$

AGN jet densities are typically $0.001\text{--}0.02 \text{ H/cm}^3$ with ambient interstellar medium densities typically $\sim 1 \text{ H/cm}^3$ within a galaxy (Antonuccio et al. 2008, Wagner et al. 2012). We take the average ambient density \bar{n}_a here to be 0.1 H/cm^3 as typical of the less dense *intergalactic* medium near the the inner filament of Cen A, and take the jet to ambient density ratio $n_j/\bar{n}_a = 0.1$. The jet power $\mathcal{P}_j = 3 \times 10^{43} \text{ erg s}^{-1}$ is representative of a low power AGN jet like Cen A: AGN jets typically have powers between 10^{43} and $10^{46} \text{ erg s}^{-1}$ (Antonuccio et al. 2008, Tortora et al. 2009, Wagner et al. 2012). The jet velocity of $4 \times 10^4 \text{ km s}^{-1} = 0.13c$ gives the correct magnitude of the power as well as the observed bow shock velocity of the Cen A jet (Crockett et al. 2012). The ambient temperature $T_a = 10^4 \text{ K}$ agrees with observations (Crockett et al. 2012), and the jet temperature $T_j = 10^5 \text{ K}$ is chosen to give pressure-matching between jet and ambient.

In order to analyze the consequences of different cloud sizes and masses, we simulated twelve clouds (arranged in lines of three centered around the jet axis as shown in Figure 2) rather than just the three observed in the inner filament of Cen A as imaged by Crockett et al. (2012).

The densities of the ambient gas and the molecular clouds were initialized (see Figure 3) using random perturbations satisfying the Kolmogorov energy spectrum of a turbulent gas (e.g., Elmegreen 2002), within the $[\rho_{\min}, \rho_{\max}]$ ranges for the ambient gas and clouds given in Table 1. The physical (x, y, z) grid was filled with random values from a normalized Gaussian distribution g , which was then transformed into Fourier wave space (k_x, k_y, k_z) to obtain \hat{g} . The transformed Gaussian was scaled by $\sqrt{k^{-5/3}}$ where $k = (k_x^2 + k_y^2 + k_z^2)^{1/2}$ to obtain $\hat{f} = \sqrt{k^{-5/3}}\hat{g}$. The unscaled density

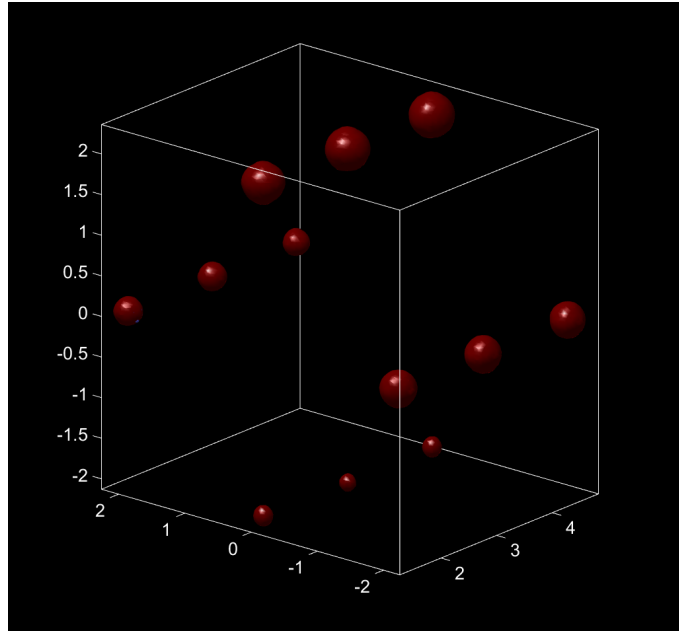


Figure 2. Twelve molecular clouds with various diameters (130–325 pc) and density ranges are arranged in lines of three centered around the jet axis. Lengths along the boundaries are in units of 10^{16} km = 324 pc.

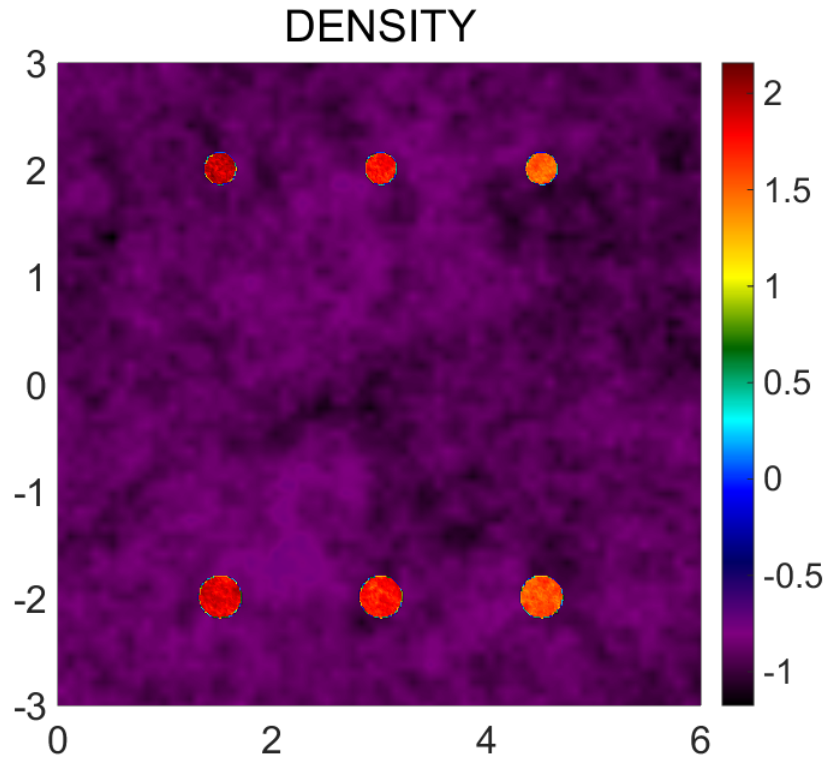


Figure 3. Initial values of logarithm of density $\log_{10}(n)$ in the xz plane showing the Kolmogorov spectrum of density perturbations, with n in H atoms/cm³. Lengths along the boundaries are in units of 10^{16} km = 324 pc.

$\tilde{\rho}$ was then calculated as the exponential of the inverse Fourier transform of \hat{f} , i.e., $\tilde{\rho} = \exp(f)$, which has a log-normal distribution with an energy spectrum satisfying $|E(k)|^2 \sim k^{-5/3}$. Finally, the scaled density ρ was defined by linearly scaling $\tilde{\rho}$ to be in the range $[\rho_{\min}, \rho_{\max}]$.

3. SIMULATION RESULTS

3.1. Jet Evolution

In the simulation figures, the jet is surrounded by a strong bow shock plus bow-shocked cocoon. The jet is propagating initially at Mach 3400 with respect to the average sound speed in the ambient gas, and Mach 1100 with respect to the sound speed in the jet gas. However, the jet tip actually propagates at an average velocity of approximately 1.2×10^4 km s⁻¹, at Mach 1000 with respect to the average sound speed in the ambient gas, since the jet is slowed down as it impacts the heterogeneous ambient environment.

The jet is emitted by the AGN at a velocity of approximately $0.3c$ (Bridle & Perley 1984), but the late time propagation velocity of the jet through the lumpy intergalactic medium is impeded down to roughly 10^4 km s⁻¹. The transverse propagation velocity of the bow shock is approximately 10^3 km s⁻¹ (Mach 85 with respect to the ambient gas), which is comparable to the extrapolated bow shock velocity of 600–900 km s⁻¹ in Crockett et al. (2012).

In the plane of the sky, the inner filament of Cen A lies 8.5 kpc from the nucleus of NGC 5128, and 2 kpc away from the AGN jet (Morganti et al. 1999), extending 2200 pc parallel to the jet, with a width of approximately 50–100 pc. The initial 500 pc of the inner filament, beginning in the southwest closest to the galaxy nucleus, comprises three major groups of extended emission labeled A, B, C in Figure 5 of Crockett et al. (2012). These three clouds were modeled in the numerical simulations, with the following caveat: we placed the clouds at a distance of 650 pc from the jet in order to simulate the impact of the bow shock on the molecular clouds in a reasonable amount of CPU time. The simulations presented here took 100,000 CPU hours on the SDSC Comet XSEDE computer cluster, using 1200 cores (50 nodes \times 24 cores/node). Moving the clouds further out to 2 kpc away from the jet and increasing the bow shock impact time with the clouds from 0.7 Myr to approximately 3 Myr would require roughly $3^4 \cdot 5$ times as long with the same spatial resolution. Note that we need at least the current spatial resolution to resolve nascent star clusters, which encompass here 4^3 grid cells. We believe that the main physical effects are captured in our current simulations, while keeping the CPU time feasible.

The molecular clouds in the inner filament were initialized to be in agreement with the estimate of Crockett et al. (2012) that the pre-ablation mass of Regions 1 and 2 in cloud A is approximately $6 \times 10^5 M_\odot$. We studied a range of initial cloud masses from 10^5 to $2 \times 10^6 M_\odot$, with diameters 130–325 pc.

3.2. Star Formation

We use the three criteria of Cen & Ostriker (1992) to test for star formation, applied to averaged values in a spherical region of radius R :

$$\nabla \cdot \mathbf{u} < 0, \quad (6)$$

$$t_{\text{cool}} = \frac{E}{|dE/dt|} = \frac{E}{C} \ll t_{\text{grav}} = \pi^{1/2} G^{-1/2} \rho^{-1/2}, \quad (7)$$

$$M_{\text{region}} = \frac{4\pi}{3} \rho R^3 > M_{\text{Je}} \equiv \frac{4\pi}{3} \rho \lambda_{\text{Je}}^3 \approx G^{-3/2} \rho^{-1/2} c_s^3 \quad (\text{Jeans unstable}), \quad (8)$$

where t_{cool} is the characteristic radiative cooling time, t_{grav} is the characteristic gravitational collapse time, M_{Je} is the Jeans mass, $\lambda_{\text{Je}} \equiv c_s t_{\text{grav}}$ is the Jeans length, and $c_s = \sqrt{\gamma P / \rho} = \sqrt{\gamma k_B T / m}$ is the sound speed. We define the Jeans ratio as $\text{Je} \equiv M_{\text{region}} / M_{\text{Je}}$. In equation (8), $\text{Je} > 1$ means the region is Jeans unstable, i.e., the gravitational free-fall time is shorter than the time needed for a pressure wave to traverse the collapsing region and bounce back, resisting collapse.

Thus the region will collapse gravitationally if $\text{Je} > 1$ and $t_{\text{cool}} \ll t_{\text{grav}}$, plus $\nabla \cdot \mathbf{u} < 0$, which is typically true in bow-shocked regions. Note that equations (7) and (8) are equivalent to

$$\frac{t_{\text{cool}}}{t_{\text{grav}}} \approx \frac{EG^{1/2}\rho^{1/2}}{C} \ll 1, \quad (9)$$

and

$$\text{Je} = \left(\frac{R}{\lambda_{\text{Je}}} \right)^3 \approx R^3 G^{3/2} \rho^{3/2} c_s^{-3} \approx R^3 G^{3/2} m^{3/2} \left(\frac{\rho}{k_B T} \right)^{3/2} > 1, \quad (10)$$

respectively. Thus star formation is facilitated by a simultaneous combination of high densities and low temperatures from equation (10), *plus* strong radiative cooling—which requires T not to be too low—from equation (9).

To identify star cluster forming regions, we first divided the computational grid into cubic cells of length D on a side, where $D = 20$ pc $= 4\Delta$ is the typical diameter of a nascent cluster. Next we averaged all state variables and $\nabla \cdot \mathbf{u}$ within each cell, and for each averaged cell, we computed the mass within the cell $M_{\text{cell}} \equiv M_{\text{region}}$, the Jeans mass M_{Je} , the cooling time t_{cool} , and the gravitational free-fall time t_{grav} . If the three conditions above for star formation held for an averaged cell (we used $t_{\text{cool}} \leq 0.2 t_{\text{grav}}$), we marked that cell as a star cluster.

For the molecular clouds considered here, $D = 20$ pc is the physically relevant length scale in that for $D = 10$ pc many adjacent star clusters form which should be merged into a single star cluster, and for $D = 30$ pc some star forming regions are suppressed by the averaging with neighboring regions that do not form stars. The computed post-ablation averaged quantities in the star clusters are given in Table 2, with 71 clusters identified in the twelve clouds when $D = 20$ pc.

Table 2. Computed ranges for averaged values in the star cluster cells at 780,000 yr, with 71 clusters identified in the twelve clouds when the cluster diameter $D = 20$ pc.

Quantity	Min Value	Max Value	Units
n	32	60	H ₂ molecules/cm ³
T	15	270	K
c_s	0.45	1.9	km s ⁻¹
t_{cool}	0.03	1.6	Myr
t_{grav}	8.7	12	Myr
$t_{\text{cool}}/t_{\text{grav}}$	0.003	0.15	
λ_{Je}	4.3	18	pc
M_{cluster}	10 ⁴	1.9×10^4	M_{\odot}
M_{Je}	200	1.6×10^4	M_{\odot}
Je	1.1	77	

4. DISCUSSION

Cross sections of the 3D numerical simulations at 780,000 yr—just after the bow shock has traversed the molecular clouds—are shown in Figure 4. Turbulent Kelvin-Helmholtz mixing of the jet and ambient gas is evident in a layer of roughly 2×10^{16} km around the jet. This layer has the lowest densities $n \approx 10^{-3.5}$ H atoms/cm³ and highest temperatures $T \approx 10^8$ – 10^{10} K; it also has a strong backflow counter to the direction of the jet flow. Post-shock ablation of the clouds is also clearly visible in Figure 4. Even though the clouds are at the lowest temperatures $T \approx 15$ – 270 K, the strongest radiative cooling (which is essential for star formation) takes place around the surfaces of the clouds. While the cloud cores are not cooling as intensely, they are at lower temperatures and higher densities than the surfaces, so star clusters form in the cloud cores as well. It is the combination of high densities, low temperatures, *and* strong radiative cooling that enables star formation.

The age of the inner lobes of Cen A is 5.6–5.8 Myr and the inner filament stars are roughly 1–3 Myr old (Crockett et al. 2012). Radio and X-ray synchrotron source lifetimes are in general on the order of 10 Myr, and therefore comfortably longer than the star formation times. The AGN jet thus exists long enough to trigger star formation in nearby molecular clouds which are large enough and dense enough; in our simulations, star formation is triggered by 780,000 yr.

Table 3 shows the initial cloud parameters and the number of star clusters formed at 780,000 yr in each cloud. What is evident from the data is that more than one star cluster forms for $D = 20$ pc only if $n_{\text{max}} \geq 50$ H₂ molecules/cm³. For $D = 20$ pc, five out of twelve clouds form a significant number of star clusters. However, recall that in the interstellar medium on average only about 10% of regions satisfying the star formation criteria actually collapse to form star clusters. What is important for our purposes is that there are a significant number of clouds that do not form star clusters, while the denser clouds do.

Figure 5 shows the xz plane slice of the cells used to identify star cluster regions for $D = 20$ pc. The locations of the nascent star clusters are indicated in Figures 6 and 7, with 71 clusters of mass $M_{\text{cluster}} = 1$ – $1.9 \times 10^4 M_{\odot}$ formed with $D = 20$ pc. The simulated clouds with approximately 20 clusters are a good match to cloud A in the *HST* images,

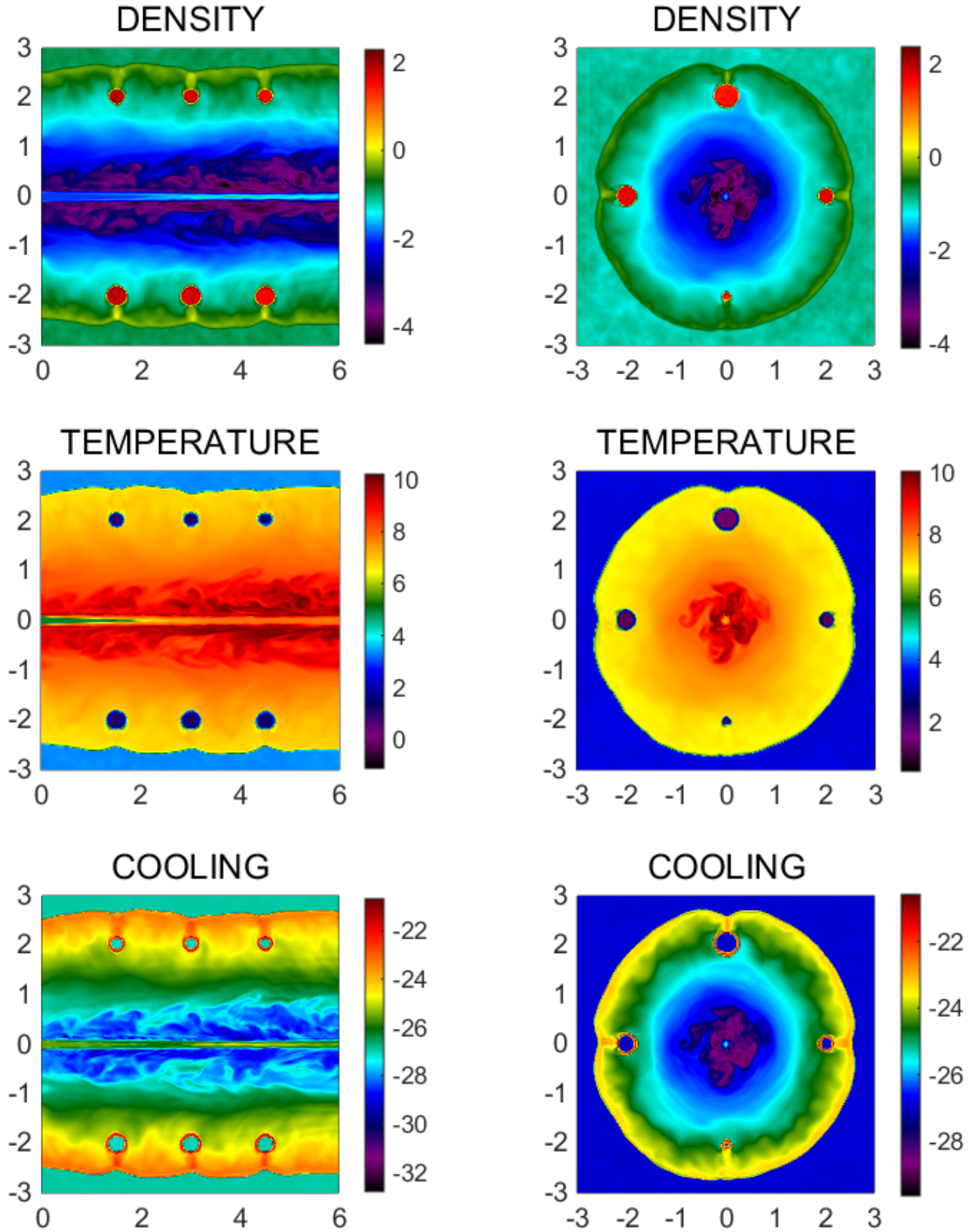


Figure 4. Logarithm of density $\log_{10}(n)$ with n in H atoms/cm³, logarithm of temperature $\log_{10}(T)$ with T in K, and logarithm of total radiative cooling $\log_{10}(C)$ with C in erg cm⁻³ s⁻¹ at $t = 780,000$ yr. Left panel: in the xz plane; right panel: in the central z -slice. Lengths along the boundaries are in units of 10^{16} km = 324 pc.

Table 3. Initial cloud parameters and the number $N_{20\text{pc}}$ of star clusters for $D = 20$ pc formed at 780,000 yr in each cloud, with $\bar{n} = 1$ H₂ molecule/cm³. For all clouds, $n_{\text{min}} = 2$ H₂ molecules/cm³. Rows are ranked by $N_{20\text{pc}}$.

Cloud	n_{max}/\bar{n}	$D_{\text{cloud}}/\text{pc}$	$M_{\text{cloud}}/(10^5 M_{\odot})$	$N_{20\text{pc}}$
1	60	260	17	29
2	75	195	9	18
3	50	195	6	10
4	50	260	15	7
5	75	130	3	4
6	50	130	2	2
7	40	325	23	1
8	30	325	18	0
9	30	260	9	0
10	25	195	3	0
11	25	130	1	0
12	20	325	12	0

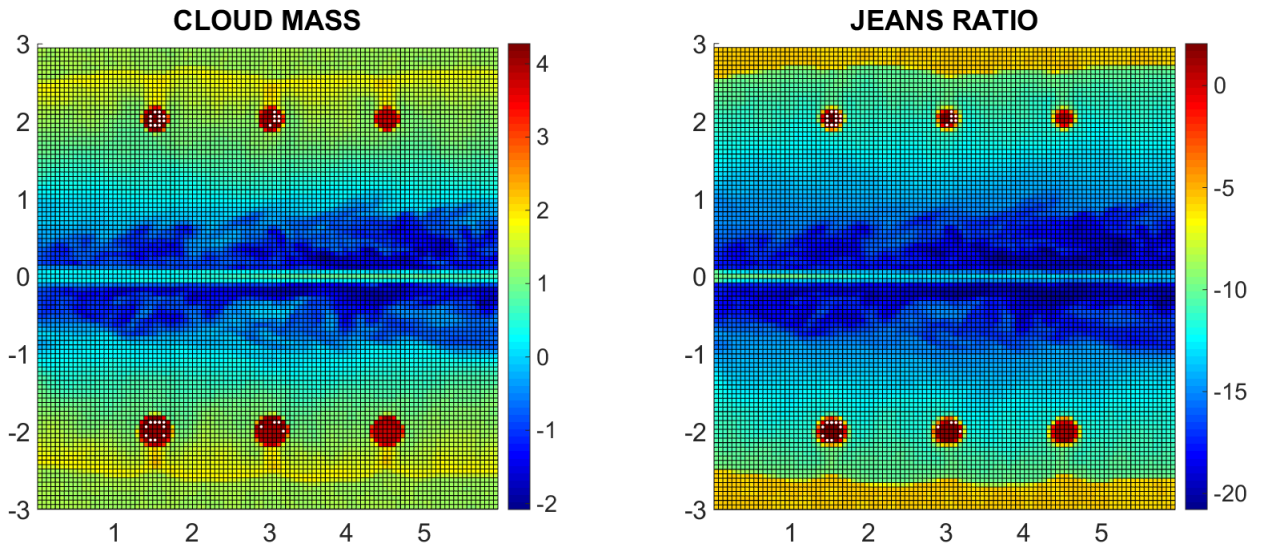


Figure 5. Left panel: $\log_{10}(M_{\text{cell}}/M_{\odot})$ in each cell, with $D = 20$ pc. Right panel: $\log_{10}(\text{Je})$ in each cell. Regions satisfying the star formation criteria are marked with white dots. Lengths along the boundaries are in units of 10^{16} km = 324 pc.

while clouds B and C show no clusters, matching several of our simulated clouds.

The star clusters in Figure 7 have already persisted to roughly $t_{\text{grav}}/10$. Persistence of the star clusters to late times on the order of $t_{\text{grav}}/3 \approx 3$ Myr was verified by cylindrically symmetric simulations with exactly the same initial parameters as in the 3D simulations and with a final time of 3 Myr. The greater density contrast evident in Figure 8 is due to the much further development of Kelvin-Helmholtz vortex rollup inside the jet cocoon. At 1 Myr there are 27 star clusters in the three spherical clouds (considered as part of the cylindrically symmetric cloud “ring” near the rz cross section), while at 3 Myr there are 30 clusters, so the number of star clusters is actually increasing slightly between 1 Myr and 3 Myr.

In Figure 9, a plot of $\log_{10}(T)$ vs. $\log_{10}(n)$ is shown for averaged cell values from the 3D simulations, demonstrating that star cluster regions require high density and low temperature. However if the temperature is too low, clusters do not form because the radiative cooling is too weak and $t_{\text{cool}} \approx t_{\text{grav}}$ (lower right-hand corner of the scatter plot).

Several regions can be clearly seen in the figure. The inner cocoon points can be seen in the “handle” shape in the upper left-hand part of the plot, with high temperatures and low densities. The points near the jet inflow can be seen as deviations from the handle near $n = n_j = 10^{-2}$ H atoms/cm³. Points in the outer parts of the cocoon and in the

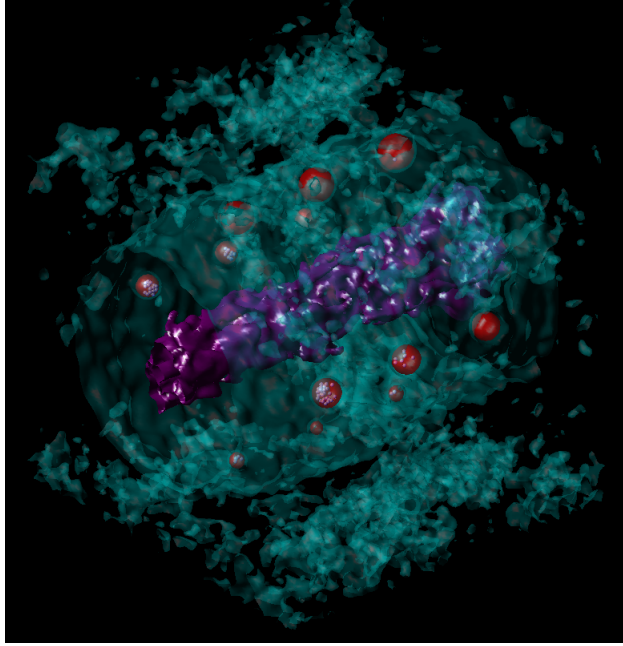


Figure 6. Density isosurfaces at $t = 780,000$ yr. Purple: low density ($n = 10^{-3}$ H atoms/cm³) jet cocoon; cyan: medium density ($n = 0.1$ H atoms/cm³) ambient and bow-shocked regions; red: high density ($n = 5$ H₂ molecules/cm³) molecular clouds. Star clusters for $D = 20$ pc are shown as white spheres.

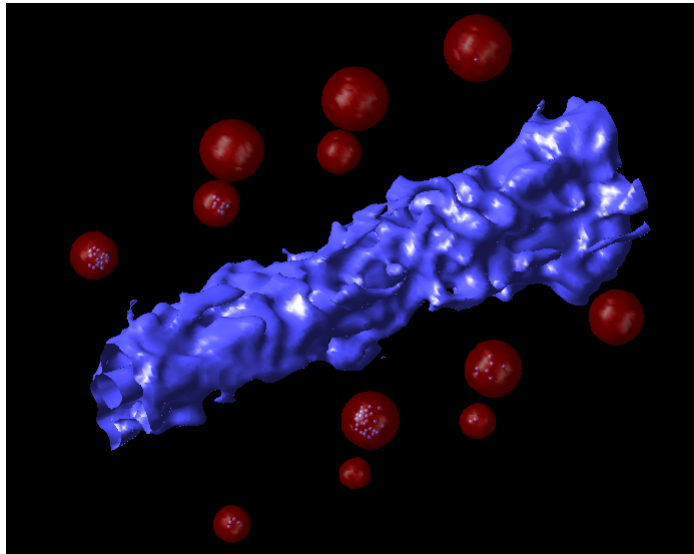


Figure 7. Density isosurfaces plus star clusters shown as white spheres. 71 clusters of mass $1\text{--}1.9 \times 10^4 M_{\odot}$ were found with $D = 20$ pc.

unshocked ambient region lie in the dense vertical strip near the average ambient density $n \approx 10^{-1}$ H atoms/cm³. The more sparsely scattered points in the rightmost region are in the molecular clouds, with the star-forming regions in the lower right-hand corner, with low temperatures and high densities.

Since $P = nk_B T$, the log-log plot of a pressure-matched gas would be a straight line with constant slope and a y -intercept of $\log P$. Two main trend lines are visible in the figure, showing two disparate pressure regimes. The lower pressure line corresponds to the original pressure of the entire region $P_j = P_a = P_c \approx 0.1$ eV cm⁻³, which includes all of the ambient points and most of the points in the molecular clouds. The higher pressure line corresponds to a pressure four orders of magnitude greater than P_j , and contains mainly the bow-shocked cocoon points. Although it is not apparent from the plot because many data points are plotted over each other, the data points lying between the

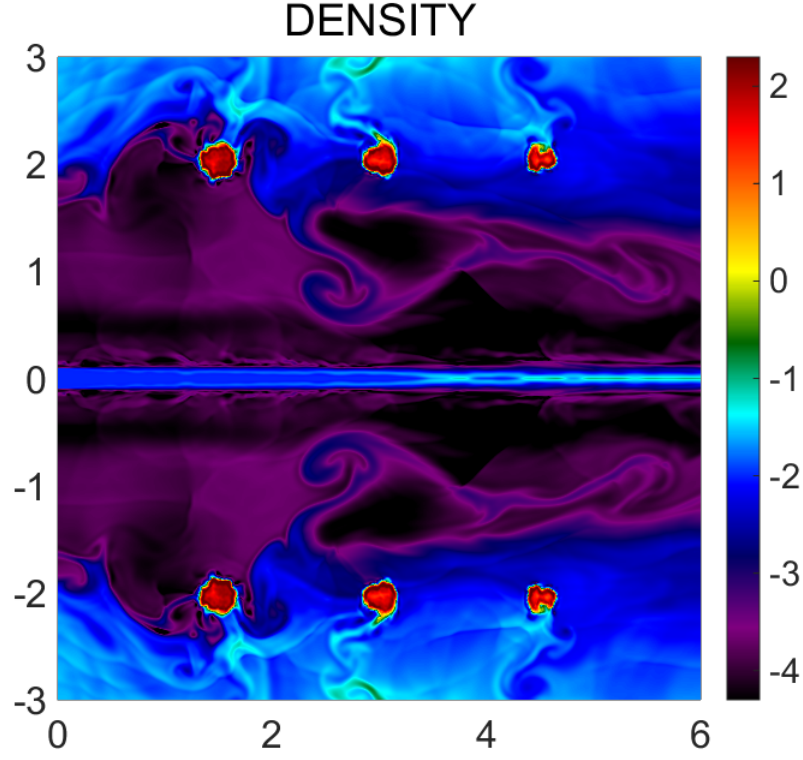


Figure 8. Logarithm of density $\log_{10}(n)$ in the rz plane at $t = 3$ Myr for a cylindrically symmetric simulation, with n in H atoms/cm³. Lengths along the boundaries are in units of 10^{16} km = 324 pc.

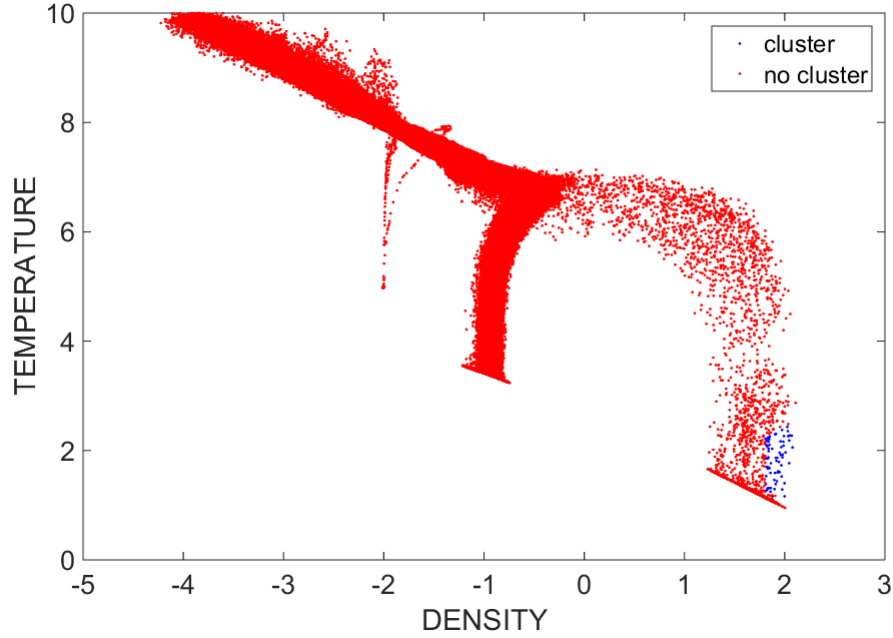


Figure 9. $\log_{10}(T)$ vs. $\log_{10}(n)$ for averaged cell values with $D = 20$ pc, with T in K and n in H atoms/cm³. The star cluster regions require high density and low temperature, and are shown by blue dots.

two pressure regimes make up only a small fraction of the total number of points and correspond to points near the boundaries of the cocoon or clouds.

5. CONCLUSION

The 3D numerical simulations demonstrate that the transverse bow shock of the Cen A jet induces star formation as it impacts surrounding dense molecular clouds. The passage of the bow shock causes the molecular clouds to undergo strong radiative cooling, thereby triggering the star formation observed in the inner filament of Cen A. We find that star clusters form inside a bow-shocked molecular cloud when the maximum initial density of the cloud is ≥ 40 H₂ molecules/cm³. In a typical molecular cloud of mass $10^6 M_{\odot}$ and diameter 200 pc, approximately 20 star clusters of mass $10^4 M_{\odot}$ are formed, matching the *HST* images of cloud A in Crockett et al. (2012).

Cross sections of the 3D numerical simulations at 780,000 yr—just after the bow shock has traversed the molecular clouds—display turbulent Kelvin-Helmholtz mixing of the jet and ambient gas in a layer of roughly 2×10^{16} km around the jet. This layer has the lowest densities $n \approx 10^{-3.5}$ H atoms/cm³ and highest temperatures $T \approx 10^8$ – 10^{10} K; it also has a strong backflow counter to the direction of the jet flow. Post-shock ablation of the clouds is also clearly visible. Even though the clouds are at the lowest temperatures $T \approx 15$ – 270 K, the strongest radiative cooling—which is essential for star formation—takes place around the surfaces of the clouds. While the cloud cores are not cooling as intensely, they are at lower temperatures and higher densities than the surfaces, so star clusters form in the cloud cores as well. It is the combination of high densities, low temperatures, *and* strong radiative cooling that enables star formation. However if the temperature is too low, clusters do not form because the radiative cooling is too weak and $t_{\text{cool}} \approx t_{\text{grav}}$.

In future work, we plan to include gravity in the 3D gas dynamical solver, and to follow a collapsing cloud with approximately 20 nascent star clusters at 780,000 yr out to $t_{\text{grav}} \approx 10$ Myr. Close examination of the composite image of Cen A in Figure 1 shows a line of blue star-forming regions, stretching from just below the tip of the X-ray jet all the way out to the inner filament, along the transverse bow shock of the jet. These star-forming regions, which we plan to model in detail in future work, would make excellent targets for further observations with the *HST WFC3*.

ES was supported by NSF grant AST14-07835 and NASA theory grant NNX15AK82G. We would like to thank the San Diego Supercomputer Center (SDSC) at the University of California, San Diego, and the Extreme Science and Engineering Discovery Environment (XSEDE) for providing HPC resources via grant TG-AST130021. RAW acknowledges support from HST grant GO-11359 from the Space Telescope Science Institute, which is operated by the Association of Universities for Research in Astronomy, Inc., under NASA contract NAS 5-26555. RAW also acknowledges support from NASA JWST Interdisciplinary Scientist grants NAG5-12460 and NNX14AN10G from GSFC.

REFERENCES

- Antonuccio-Delogu, V., & Silk, J. 2008, *MNRAS*, 389, 1750
- Bicknell, G. V., Sutherland, R. S., van Breugel, W. J. M., et al. 2000, *ApJ*, 540, 67
- Bridle, A. H., & Perley, R. A. 1984, *ARA&A*, 22, 319
- Brinchmann, J., & Ellis, R. S. 2000, *ApJ*, 536, L77
- Cavagnolo, K. W., Donahue, M., Voit, G. M., & Sun, M. 2009, *ApJS*, 182, 12
- Cen, R., & Ostriker, J. P. 1992, *ApJ*, 399, L113
- Costa, T., Sijacki, D., & Haehnelt, M. G. 2014, *MNRAS*, 444, 2355
- Cowie, L. L., & Barger, A. J. 2008, *ApJ*, 686, 72
- Cowie, L. L., Songaila, A., Hu, E. M., & Cohen, J. G. 1996, *AJ*, 112, 839
- Crockett, R. M., Shabala, S. S., Kaviraj, S., et al. 2012, *MNRAS*, 421, 1603
- Croft, S., van Breugel, W., de Vries, W., et al. 2006, *ApJ*, 647, 1040
- Croton, D. J., Springel, V., White, S. D. M., et al. 2006, *MNRAS*, 365, 11
- Dey, A., van Breugel, W., Vacca, W. D., & Antonucci, R. 1997, *ApJ*, 490, 698
- Dugan, Z., Bryan, S., Gaibler, V., Silk, J., & Haas, M. 2014, *ApJ*, 796, 113

- Dugan, Z., Gaibler, V., Silk, J. 2016, arXiv:1608.01370
- Dunn, R. J. H., & Fabian, A. C. 2006, MNRAS, 373, 959
- Elmegreen, B. G. 2002, ApJ, 564, 773
- Fabian, A. C. 2012, ARA&A, 50, 455
- Fassett, C. I., & Graham, J. A. 2000, ApJ, 538, 594
- Feain, I. J., Ekers, R. D., Murphy, T., et al. 2009, ApJ, 707, 114
- Gaibler, V. 2014, AN, 335, 531
- Gaibler, V., Khochfar, S., Krause, M., & Silk, J. 2012, MNRAS, 425, 438
- Gardner, C. L., & Dwyer, S. J. 2009, AcMaS, 29B, 1677
- Gaspari, M., Brighenti, F., & Temi, P. 2012a, MNRAS, 424, 190
- Gaspari, M., Ruszkowski, M., & Sharma, P. 2012b, ApJ, 746, 94
- Gopal-Krishna, & Wiita, P. J. 2010, NA, 15, 96
- Granato, G. L., De Zotti, G., Silva, L., Bressan, A., & Danese, L. 2004, ApJ, 600, 580
- Graham, J. A., & Fassett, C. I. 2002, ApJ, 575, 712
- Ha, Y., Gardner, C. L., Gelb, A., & Shu, C.-W. 2005, JSCoM, 24, 29
- Hu, X. Y., Adams, N. A., & Shu, C.-W. 2013, JCP, 242, 169
- Israel, F. P. 1998, ARA&A, 8, 237
- Hopkins, A. M., & Beacom, J. F. 2006, ApJ, 651, 142
- Hopkins, P. F., Hernquist, L., Cox, T. J., et al. 2006, ApJS, 163, 1
- Johansson, P. H., Naab, T., & Ostriker, J. P. 2012, ApJ, 754, 115
- Karachentsev, I. D. et al. A&A, 2002, 385, 21
- Karim, A., Schinnerer, E., Martínez-Sansigre, A., et al. 2011, ApJ, 730, 61
- Kraft, R. P., Forman, W. R., Hardcastle, M. J., et al. 2009, ApJ, 698, 2036
- Le Bourlot, J., Pineau des Forêts, G., & Flower, D. R. 1999, MNRAS, 305, 802
- Li, Y., Bryan, G. L., Ruszkowski, M., et al. 2015, ApJ, 811, 73
- McNamara, B. R., & Nulsen, P. E. J. 2007, ARA&A, 45, 117
- Minkowski, R. 1958, PASP, 70, 143
- Morganti, R., Killeen, N. E. B., Ekers, R. D., Oosterloo, T. A. 1999, MNRAS, 307, 750
- Morganti, R., Robinson, A., Fosbury, R. A. E., et al. 1991, MNRAS, 249, 91
- Noeske, K. G., Faber, S. M., Weiner, B. J., et al. 2007, ApJ, 660, L47
- Peterson, J. R., Paerels, F. B. S., Kaastra, J. S., et al. 2001, A&A, 365, L104
- Rafferty, D. A., McNamara, B. R., Nulsen, P. E. J., & Wise, M. W. 2006, ApJ, 652, 216
- Rejkuba, M., Greggio, L., & Zoccali, M. 2004, A&A, 415, 915
- Rejkuba, M., Minniti, D., Courbin, F., & Silva, D. R. 2002, ApJ, 564, 688
- Rejkuba, M., Minniti, D., Silva, D. R., & Bedding, T. R. 2001, A&A, 379, 781
- Richardson, M. L. A., Scannapieco, E., Devriendt, J., et al. 2016, ApJ, 825, 83
- Saxton, C. J., Sutherland, R. S., & Bicknell, G. V. 2001, ApJ, 563, 103
- Scannapieco, E., & Oh, S. P. 2004, ApJ, 608, 62
- Scannapieco, E., Silk, J., & Bouwens, R. 2005, ApJ, 635, L1
- Schmutzler, T., & Tscharnuter, W. M. 1993, A&A, 273, 318
- Shu, C.-W. 1999, High-Order Methods for Computational Physics, Vol. 9 (New York: Springer)

- Silk, J. 2013, *ApJ*, 772, 112
- Somerville, R. S., Hopkins, P. F., Cox, T. J., Robertson, B. E., & Hernquist, L. 2008, *MNRAS*, 391, 481
- Sutherland, R. S., Bicknell, G. V., & Dopita, M. A. 1993, *ApJ*, 414, 510
- Tortora, C., Antonuccio-Delogu, V., Kaviraj, S., Silk, J., Romeo, A. D., & Becciani, U. 2009, *MNRAS*, 396, 61
- van Breugel, W., Filippenko, A. V., Heckman, T., & Miley, G. 1985, *ApJ*, 293, 83
- Wagner, A. Y., Bicknell, G. V., & Umemura, M. 2012, *ApJ*, 757, 136
- Wagner, A. Y., Bicknell, G. V., Umemura, M., Sutherland, R. S., & Silk, J. 2016, *AN*, 337, 167
- Wurster, J., & Thacker, R. J. 2013, *MNRAS*, 431, 2513
- Zinn, P.-C., Middelberg, E., Norris, R. P., & Dettmar, R.-J. 2013, *ApJ*, 774, 66